Shape dependence of photosensitive properties of WO3 oxide for photocatalysis under solar light irradiation

Margaux Desseigne, Nadine Dirany, Virginie Chevallier, Madjid Arab

Shape dependence of photosensitive properties of WO_3 oxide for photocatalysis under solar light irradiation

Margaux Desseigne*[a], Nadine Dirany[a,b], Virginie Chevallier[a], Madjid Arab*[a]

[a] Université de Toulon, Aix Marseille Université, CNRS, IM2NP, Toulon ou Marseille, France
[b] Université Libanaise - Ecole doctorale des sciences et technologie, Beyrouth - Liban

*Correspondance e-mail : margaux.desseigne@univ-tln.fr ; madjid.arab@univ-tln.fr

Abstract

Two morphologies of nanostructured WO_3, nanoplatelets (NP) and pseudospheres (PS), were synthesized using a simple chemical route. The obtained powders were structurally characterized using thermal analyses and a combined XRD with Rietveld refinement. Their morphological and growth mechanisms were followed by SEM during the maturation phase. The results showed a square/rectangular shape and pseudospherical morphology, which exhibited a monoclinic phase after calcination at 400°C and an orthorhombic phase after calcination at 500°C. The temperature treatment induced an increase of grain size for the NP lateral size, while the PS size remains temperature independent. The photocatalytic activity was evaluated by the degradation of methylene blue under solar light irradiation. The degradation process was investigated by studying the photosensitive properties, optical absorption, photoluminescence and photoresistance. The photodegradation activity of methylene blue is composed of a rapid and strong adsorption step followed by a photoinduced catalytic process. The PS sample revealed a higher adsorption rate than NP powders at the low calcination temperature, while the photoinduced catalysis is better at the high calcination temperature, reaching 88% at 500°C. The photosensitive properties showed a low luminescence intensity and a long charge carrier recombination time, thus indicating the photocatalytic efficiency of the elaborated samples.

Keywords: Tungsten trioxide; morphology; methylene blue; photocatalysis; photoluminescence; photoresistance.

1. Introduction

Several research efforts have been devoted to using functional semiconducting materials for environmental applications [1,2]. Therefore, improving and modulating properties is one of the challenging research pathways in this field. The chemical and physical properties of materials are strongly dependent on their structure, crystallite size and morphology [3–6]. In recent years,

several micro-nano structured materials have been obtained with various morphologies and variable dimensions (1D, 2D and 3D) [7,8]. These architectures favour the surface to volume ratio, compared to the bulk material, and give rise to various surface states with different surface energies. Among these functional materials, nanostructured tungsten oxide is a prominent metal oxide. WO_3 has been considered as a promising candidate for several applications, such as gas sensors [9], electrochromic and photochromic devices [10], photoelectrodes [11,12], field emissions [13], photocatalysts [14,15], dye-sensitized solar cells and solar energy devices [16]. As an n-type indirect band gap (Eg) semiconductor, with Eg ranging from 2.6 to 3.2 eV [17], WO_3 is suitable for visible or sunlight irradiation in photocatalytic applications (as an alternative to TiO_2). Furthermore, tungsten oxide is chemically inert and has a good photo and thermal stability. Until now, several studies were reported on complex organic dyes photodegradation (methylene blue (MB), rhodamine B, methyl orange, congo red, etc) which are present in wastewater from the textile [18,19]. Their treatment is a major issue for environmental protection. Different structures with elementary shapes or self-assembled structure like nanorods, cubes, sheets and spheres have been reported as a photocatalyst for dyes [20–23]. Nevertheless, there are few data reporting the influence of WO_3 grains shape and size on their photocatalytic properties. It has been noticed that the morphology based on structure exhibits more advantages in photocatalytic application due to the charge separation, surface reaction and surface light absorption.

In the case of MB photodegradation, the reported results indicate that sometimes only the photoinduced degradation mechanism occurs, [24–26] while other studies revealed only the adsorption process [27]. Vamvasakis et al. reported MB photodegradation over WO_3 nanostructure, indicating a rapid photocatalysis process until complete decomposition [28]. They observed a transformation of MB into Bernthen's Methylene Violet (MBV). Zhang et al. indicated both adsorption and photocatalysis processes; in such cases, the adsorption rate reaches an important part of [25] photodegradation. Otherwise, Adhikari et al. [29] and Guan et al. [30] reported that WO_3 behaves as high adsorbent of MB. These results were obtained using several WO_3 flower-like shapes based on nanosheets, spheres and nanoplates. So, it appears that there are different behaviours for MB (cationic dye) onto WO_3 oxides (negative state surface) despite their strong electrostatic interaction. Furthermore, some WO_3 powders are regenerated after several washings with additional treatment, while others undergo an irreversible adsorption process.

This work was motivated by two focus. On one hand, the purpose was to show the role of two WO_3 shapes (anisotropic nanoplates and isotropic pseudospheres) on the MB degradation. On the other hand, the interest was to compare the dye's ratio of adsorption and photocatalysis during the degradation process between two morphologies treated at three calcination temperatures. The material structure, morphological evolution and growth mechanism were characterized in detail by SEM, TEM and XRD analyses. The relationship between structure, morphology and photocatalytic activity was investigated according to the photosensitive properties: adsorption, optical band gap, photoluminescence and photoresistance.

2. Materials and methods

2.1. *Materials*

The tungsten oxide precursors $Na_2WO_4.2H_2O$ and $(NH_4)_{10}(W_{12}O_{41}).6H_2O$ were purchased from Sigma Aldrich and used without any purification. Acid solutions, 37% HCl and 70% HNO_3, were obtained from Fisher Scientific. All the synthesis and characterizations using water were carried with 18 MΩ deionized water.

2.2. *Synthesis methods of WO_3*

The nanoplatelets (NP) and pseudospheres (PS) WO_3 particles were synthesized with sodium tungsten dihydrate $Na_2WO_4.2H_2O$ and ammonium tungstate hexahydrate $(NH_4)_{10}(W_{12}O_{41}).6H_2O$, respectively, as precursors by using a simple free template precipitation method. The synthesis details of NP and PS are reported in our previous works [31,32]. The obtained yellow precipitate was filtered, washed with distilled water and absolute ethanol several times and finally calcined at 300°C, 400°C and 500°C for 2 h in air, with a heating rate of $5°C.min^{-1}$. The WO_3 samples obtained after those thermal treatments were labelled NP300, NP400, NP500 (nanoplatelets calcined at 300, 400 and 500°C, respectively) and PS300, PS400 and PS500 (pseudospheres calcined at 300, 400 and 500°C, respectively).

2.3. *Structural and morphological characterizations*

The WO_3 powders with two morphologies were structurally examined by XRD using an EMPYREAN Panalytical diffractometer, equipped with a copper X-ray source (wavelength λ=1.5440 Å, voltage=45 kV, intensity I=35 mA), a Ni filter eliminating K_β radiation and a Pixcel-1D-Detector. XRD analysis was carried out using the θ-2θ configuration, with a step

size of 0.0263° and a scan speed of 0.001° $2\Theta.s^{-1}$. All samples were compacted powders in a specific sample holder.

The crystallite sizes were evaluated from the corrected full width at half maximum (FWHM) of the diffraction peaks using the simplified Debye-Scherrer equation, $D = \frac{K\lambda}{\beta \cos\theta}$ where D is the crystallite size, K is the form factor (K=0.9 for gaussian profiles), λ is the X-ray radiation wavelength (λ=0.15406 nm), β is the angular broadening of Bragg peaks resulting from the size effect and θ is the Bragg angle. The integral breadth value was calculated using a gaussian approximation of peaks profiles such as $\beta^2 = \Delta(2\theta)^2_{samp} - \Delta(2\theta)^2_{stand}$. $\Delta(2\theta)_{samp}$ and $\Delta(2\theta)_{stand}$ are the Bragg peak FWHM of the synthesized samples and the standard WO_3 sample obtained after a thermal treatment of 24 h at 1000°C, respectively.

The as-prepared primary powder was submitted to thermal and thermogravimetric analyses using a SETARAM TGA/DTA 92. The thermal decomposition was studied under air, in the 25-800°C temperature range with a heating/cooling rate of 5°C.min^{-1}.

The morphologies of the WO_3 samples were observed using a SUPRA 40Vp Gemini Zeiss scanning electron microscope (SEM) operated at 5 kV. All particle sizes were determined using the Image-J software.

The UV-Visible diffuse reflectance spectra (DRS) of different samples were recorded using a LAMBDA 190s UV/Vis/NIR spectrometer along with a 150 mm integrating sphere and using $BaSO_4$ as background reference. A small volume powder sample was compacted in a manual press into a 1.2 cm powder cup and clamped on the external port of the integrating sphere. The measurements were performed at room temperature with a resolution of 0.08 nm. The baseline was determined using a calibrated reflectance standard to obtain a reflectance accuracy of 0.5%.

2.4. *Photocatalytic evaluation*

The typical procedure for the photocatalytic degradation of methylene blue MB was as follows: 20 mg of WO_3 was dissolved in 100 mL of MB solution (1×10^{-5} M), giving a suspension with pH 5.5. The solution was sonicated for 10 min and stirred in the darkness for the time necessary to reach the adsorption-desorption equilibrium between the WO_3 and MB-dye. The solution was subsequently exposed to solar light irradiation provided by Philips lamps (300 W) fixed on a removable tray while stirring the solution with a magnetic stirrer. At specified time intervals, 2 mL of the suspension were collected and centrifuged for 10 min at

13 400 rpm to remove WO_3 powder. The evolution of the MB degradation was followed with Shimadzu™ UV 2600 spectrophotometer by recording the absorbance in the 200-800 nm wavelength range, with a photometric accuracy of 0.002 abs. To further investigate the role of other active species in the photocatalytic process, disodium ethylenediaminetetraacetate (EDTA-Na, a scavenger of h^+), isopropanol (IPA, a scavenger of $^*OH$), 1,4-benzoquinone (BQ, a scavenger of $^\bullet O_2$) were used.

2.5. *Photosensitive measurement*

Photoluminescence: The equipment used to perform the luminescence measurements under UV is a Horiba Jobin-Yvon HR800 LabRam spectrometer, spatially resolved to 0.5 µm. The entrance slit, positioned behind the filter, is a diaphragm whose diameter can range from 50-500 µm. The spherical mirror, characterized by an 800 mm focal length, allows reflecting the scattered radiation from the input to the dispersive grating to the obtain spectra slot. The 364.5 nm line of an Ar-ion laser was used as the excitation source. The power which was applied at the samples was fixed to 5 µW with an acquisition time set to 100 ms.

Photoresistance: The resistance of the samples is measured using a Keithley digital multimeter, which recorded the data as a function of time. The PS and NP WO_3 powders were dispersed in solution and deposited dropwise on the surface of a SiO_2/Si wafer covered with Pt electrodes. The electrodes are arranged in interdigitated combs favouring a better contact with the WO_3 oxides. Both samples were dried at room temperature and then treated at 500°C. The resistance changes were obtained after exposure to solar radiation for 90 sec, then followed by measurements in the dark.

3. Results and discussion

3.1. *Thermogravimetric and structural characterization of samples*

Fig. 1 shows the TGA and DTA plots recorded from the two yellow precipitates synthesized as precursors for NP and PS. They revealed thermal decompositions consisting of several stages, particularly for PS. In the case of the NP precursor, the first step occurred below 125°C and corresponded to a slight weight loss of ca. 0.4%. This mainly results from the desorption of the adsorbed water in the primary powder. A second weight loss of ca. 7.2% occurred between ca. 150 and 300°C and it is due to the elimination of interstructural water molecules. The first phase formed during crystallization is orthorhombic tungstite $WO_3.H_2O$, as reported in literature [33] and confirmed by the recorded XRD pattern of the powder obtained after the

maturation step but before calcination (Fig. S1 ESI). Above 300°C, there is no further decomposition for this sample. However, for the PS precursor, the thermal behaviour is more complex. A first weight loss of ca. 7.1%, which occurred below 120°C, can be attributed to the evaporation of adsorbed water. The desorption step is much more significant for the pristine PS precipitate than for the NP, indicating that the former is much more sensitive to water adsorption. The desorption step is followed by three additional weight losses. The first one occurred between 170 and 270°C and reached 9.7% weight loss. It is probably related to the decomposition of organic derivatives of ammonia/nitrocompounds. The second observed exothermic peak may correspond to the oxidation of nitrogen. From 270 to 420°C, two supplementary weight losses, each 2.1%, are successively observed. The first one is accompanied by a large endothermic peak, while the second is associated with several minor endo or exothermic peaks. The last loss should be due to the removal of residual hydroxylic groups.

Above 300°C and 450°C, respectively for NP and PS, the mass stabilized. For both samples, an endothermic peak can be noted, starting at ca. 470°C and indicating a phase change. In the literature, it is widely reported that bulk WO_3 undergoes a reversible monoclinic (γ) to orthorhombic (β) phase transition around 330°C, the orthorhombic phase being then thermally stable until 740°C [17,34,35]. In Salje's earlier work [36], the γ→β transition of bulk WO_3 was reported to occur at ca. 467°C, which is consistent with the TGA/DTA results reported in this work. It is well known that the phase transition behaviour in nanostructured WO_3 greatly depends on the material's morphology, the nanostructure synthesis process and the initial precursors used. But generally, the transition temperatures are lowered for nanostructured materials compared to bulk ones [37]. This effect is reported to be correlated with the enhancement of the system surface energy induced by the crystallite size [17,37]. Here, the γ→β transition temperature is increased for both morphologies. In view of the TGA/DTA results, different calcination temperatures (300, 400 and 500°C) were systematically tested for both morphologies. The calcined samples were cooled slowly (oven inertia) to room temperature before their X-ray diffractograms were recorded.

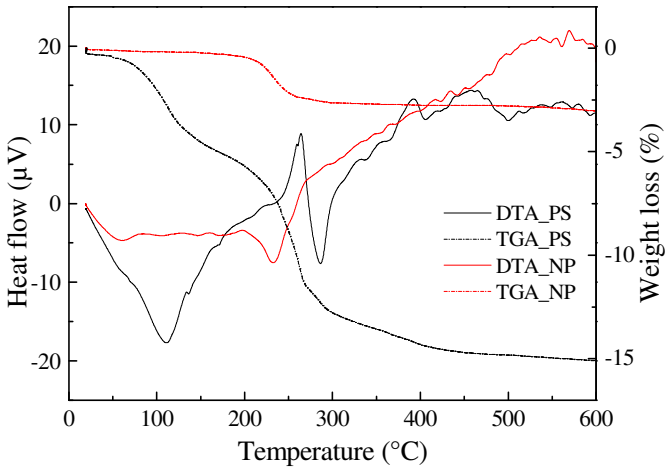

Fig. 1. TGA/DTA analyses of the thermal decomposition of primary precursor during PS and NP WO_3 formation

Fig. 2 shows the experimental patterns obtained for the six samples, along with the simulated diffractograms of both monoclinic and orthorhombic bulk WO_3 form data sheets. The two phases have very similar structures consisting of tridimensional networks of corner-sharing WO_6 octahedra. They essentially differ by the tilting orientation of the octahedra, described with respect to the ideal ReO_3-type cubic structure, characterized by the absence of tilting whatever the Cartesian (or perovskite) axes. For the β-form, there is no tilting in the [100] direction, an in-phase (or clockwise) tilting in the [010] direction, and an out of phase (or anticlockwise) tilting in the [001] direction [35]. According to the Glazer notation, the tilt system is then ($a^0b^+c^-$) for β-WO_3, while it is ($a^-b^0c^+$) for γ -WO_3. These minor changes in the octahedral tilting result in very close lattice parameters (cf. Fig. S2 ESI): *i)* for the monoclinic structure (ICSD N°050727), the space group is $P12_1/c$ N°14, with a=7.3271 Å, b=7.5644 Å, c=7.7274 Å and α=δ=90° and β= 90.488°; *ii)* for the orthorhombic phase (ICSD N° 000836), the space group is Pmnb N°62, with a=7.3410 Å, b=7.5700 Å, c=7.7540 Å and α=β=δ=90°. Fig. 2a and Fig. 2e show that the two simulated diffractograms exhibit only very slight differences. Except for the PS300 (Fig. 2b', for which TGA/DTA analysis showed that the decomposition was not achieved), the diffractograms correspond to a well crystallized tungsten oxide phase. No residual peaks (impurities) were identified, indicating the high purity of our powder. However, as our samples consist of nanostructured powders, the broadening of the peaks due to small crystallites requires Rietvield refinements to allow the accurate determination of samples' structure. The crystallographic parameters and reliability factors obtained for all samples after Rietveld refinements are summarized in Table. 1. As expected with TGA/TDA results, a structure modification occurred between 400°C and 500°C during the

calcination process. For both morphologies, the monoclinic phase was obtained at 300°C and 400°C while samples exhibited the orthorhombic phase at 500°C. This orthorhombic structure is retained after cooling at room temperature. Similar results show that post-calcined nanostructured β-WO_3 can retain a metastable orthorhombic structure once cooled at room temperature [32,38–40]

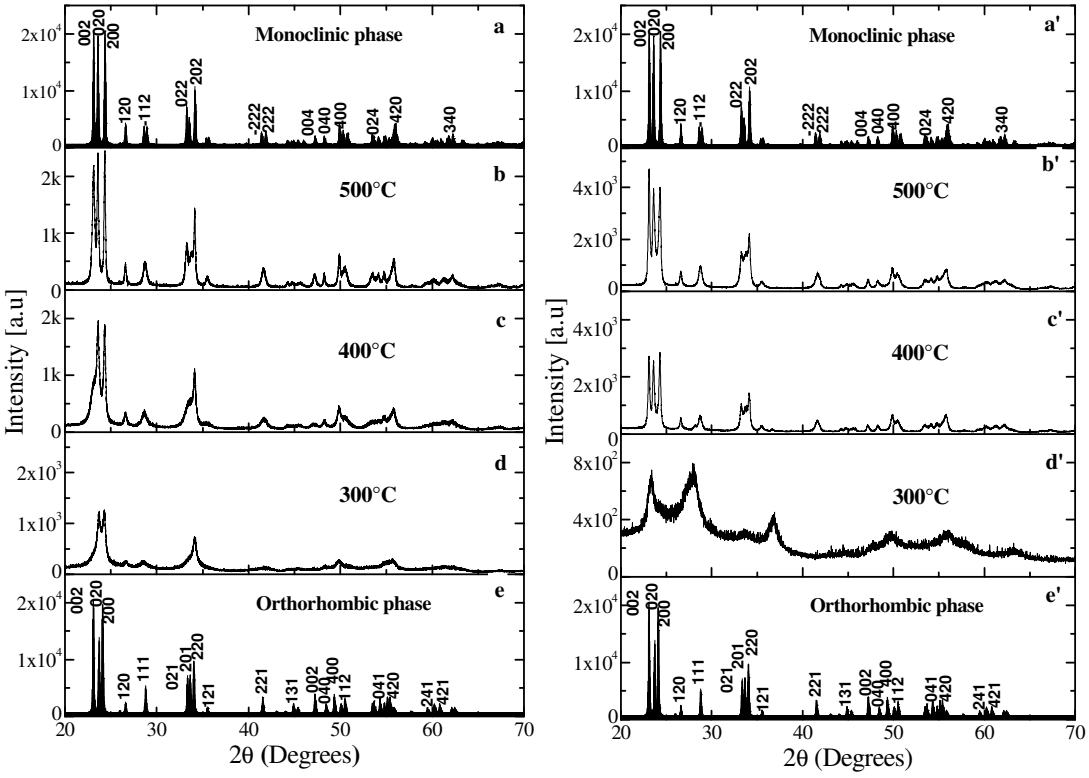

Fig. 2. X-Ray Diffraction patterns of WO_3 powders, (b to d) for NP and (b' to d') for PS calcined at different temperatures compared to the monoclinic (a,a')/orthorhombic (e,e') simulated ICSD data sheets

Table. 1. Crystallographic parameters and reliability factors determined from Rietveld refinement for PS and NP samples calcined at 400 and 500°C [32]

T (°C)	Phase	Parameters	NP	PS
400	Monoclinic	Structural parameters	a = 7.3188(0) Å	a = 7.3161(3) Å
			b = 7.5287(6) Å	b = 7.5385(1) Å
			c = 7.3930(2) Å	c = 7.4725(5) Å
			α = γ = 90.0°	α = γ = 90.0°
			β = 90.8°	β = 90.0°
		Reliability factors	R_{exp} = 7.518 %	R_{exp} = 9.096 %
			R_p = 8.104 %	R_p = 9.128 %
			R_{wp} = 10.504 %	R_{wp} = 11.717 %
			χ^2 = 1.953	χ^2 = 1.149
500	Orthorhombic	Structural parameters	a = 7.3152(3) Å	a = 7.5348(2) Å
			b = 7.6954(2) Å	b = 7.3143(2) Å
			c = 7.5366(5) Å	c = 7.6947(0) Å
			α = γ = β = 90.0°	α = γ = β = 90.0°
		Reliability factors	R_{exp} = 6.019 %	R_{exp} = 6.121 %
			R_p = 9.493 %	R_p = 9.265 %
			R_{wp} = 12.508 %	R_{wp} = 11.993 %
			χ^2 = 4.318	χ^2 = 3.838

A detailed analysis of the diffractograms shows that the peak intensities increase with temperature while the FWHM decreases. Consequently, the grains size and the degree of crystallization increase when the calcination temperature is raised. The exploitation of the XRD patterns, using the Debye-Scherrer relation, gives a crystallite size average for NP and PS samples treated at 400°C and 500°C, as presented in Table. 2. For PS samples, as the grains have no specific shape, the mean crystallite size was calculated with an average of all (hkl) reflections observed on the patterns. No calcination temperature influence could be detected with a constant 27 nm mean crystallite size. As for NP samples, in view of their square-nanoplatelets morphology, three mean crystallite sizes were calculated, from the FWHM of the three most intense peaks. They correspond to the (020), (002) and (200) reflections (in increasing 2θ-values order), both in γ- or β-phase. Note the inversion of Miller indices of the two peaks at 2θ=22.82° and 2θ=23.50° in comparison to the ICSD datasheets relative to γ- and β-phases. This is due to the respective values of b- and c-parameters given by the Rietveld refinements, b being the longest parameter in our samples (instead of c in the datasheets). For the NP400 sample, the (020) peak appears only as a shoulder at the left side of the (002) peak. Consequently, Debye-Scherrer exploitation required the deconvolution of two peaks, which induced uncertainties in the calculations. Furthermore, it is obvious that the mean crystallite size in the b-direction is smaller than in the a- and c- directions. This is consistent with our

previous electronic diffraction results [31] which showed that the short axis of the monocrystalline platelets corresponds to the b-crystallographic axis of the orthorhombic and monoclinic unit-cells. Moreover, the mean crystallite size along the b-direction is temperature-independent, while the lateral sizes (along the a- and c-directions) increase with the calcination temperature. It seems that increasing the temperature induces a growth of the nanoplatelets along the directions of the square faces only.

Table. 2. Mean crystallite sizes as a function of the calcination temperature and the morphology of WO_3 samples, as determined by the Debye-Scherrer relation from the XRD patterns

	NP		**PS**	
T (°C)	XRD peaks	Crystallite Size (nm)	XRD peaks	Crystallite Size (nm)
400	(020)	25	Average over all (hkl) peaks	27
	(002)	27		
	(200)	32		
500	(020)	26	Average over all (hkl) peaks	27
	(002)	41		
	(200)	49		

Fig. S3 (ESI) compares the morphology and size of the samples calcined at different temperatures. The corresponding histograms are presented in Fig. S4 (ESI). For NP, increasing the calcination temperature induces a significant enlargement of the platelets' lateral size, ca. 168 nm at 300°C, ca. 188 nm at 400°C and ca. 612 nm at 500°C. This tendency is consistent with the results obtained from the Debye-Scherrer analyses from XRD patterns.

3.2. *Morphological investigation*

Fig. 3 shows the SEM and TEM (inserts) images of the WO_3 powders obtained by the two synthesis methods after calcination at 500°C. They confirmed that each synthesis method leads to well crystallized grains with the expected morphology: square NP for the first synthesis (Fig. 3a) and PS grains for the second one (Fig. 3b). The platelet sample presents a relatively uniform size distribution compared to the pseudospherical powder.

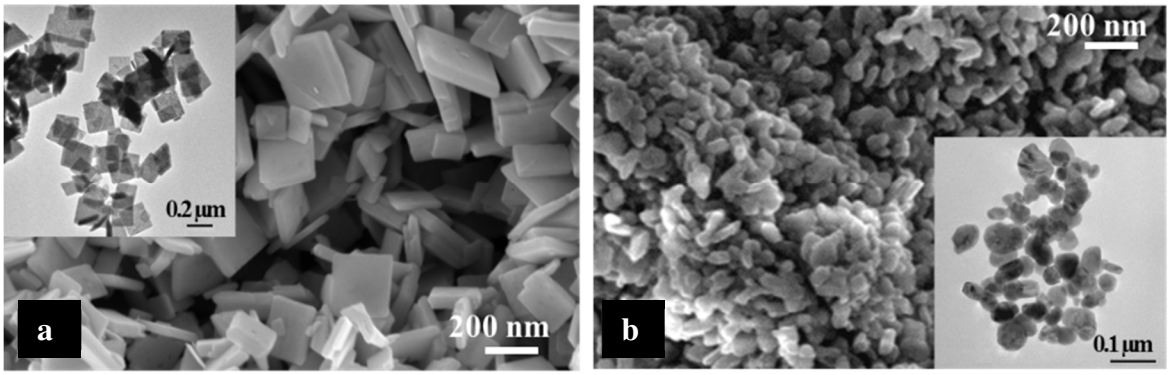

Fig. 3. SEM images of WO_3 powders obtained by a) the NP synthesis method and b) the PS synthesis method after calcination at 500°C. Inserts are TEM images of the same samples

To better understand the growth mechanism of the oxides, particularly for the nanoplatelet morphology which was obtained without surfactant, we conducted a series of time-dependent experiments. Compared to PS, NP had an additional stage of ageing at 80°C, called the maturation step, which is required before calcination. For this reason, samples were taken from the yellow precipitate at different times during the 96 hours of maturation to investigate the platelet growth mechanism. After washing and drying in the same conditions as for a complete maturation time, samples were characterized by SEM. Fig. 4 shows the morphological evolution of the powders with maturation time. Table. 3 shows the statistical characteristics of the grain size populations as a function of maturation time and the corresponding histograms are shown in Fig. S5 (ESI). To complete this study, the XRD pattern of the yellow precipitate obtained after 96 hours of maturation is presented in Fig. S1 (ESI) and it indicated a crystalline tungstite powder. As already mentioned, all reflections can be indexed in the orthorhombic structure of $WO_3.H_2O$, space group Pmnb n° 62, ICSD datasheet n° 201806. Fig. 4a) indicated that grains already have a platelet shape before ageing at 80°C, even if these platelets are irregular and not yet well facetted. The platelets lateral size are polydisperse. Extending maturation time results initially in a rapid enlargement of the mean lateral size of the platelets to roughly 200 nm accompanied by an increase of the well-faceted (square) population. The first step extends until 6 hours. Thereafter, the mean lateral size remains almost constant at around 170 nm whatever the ageing time, as shown by the histograms (Fig. S5 ESI and Table. 3). Huang and co-workers [41] also obtained square nanoplates of $WO_3.H_2O$ They reported that the square nanoplates size ranged from 100 to 200 nm with a uniform thickness of 26 nm, indicating that the plate growth was strictly extended in the 2D plane throughout the whole growing process. They suggested a model growth mechanism implying *i*) the formation of $WO_3.H_2O$ sol, *ii*) nucleation of tungstite nuclei of orthorhombic structure, and *iii)* aggregation of nuclei in two-dimensional tungstite nanoplates through six fold coordinated W^{6+} and

subsequent oxolation. In our investigations, nanoplatelets display thicknesses ranging from 20 to 70 nm.

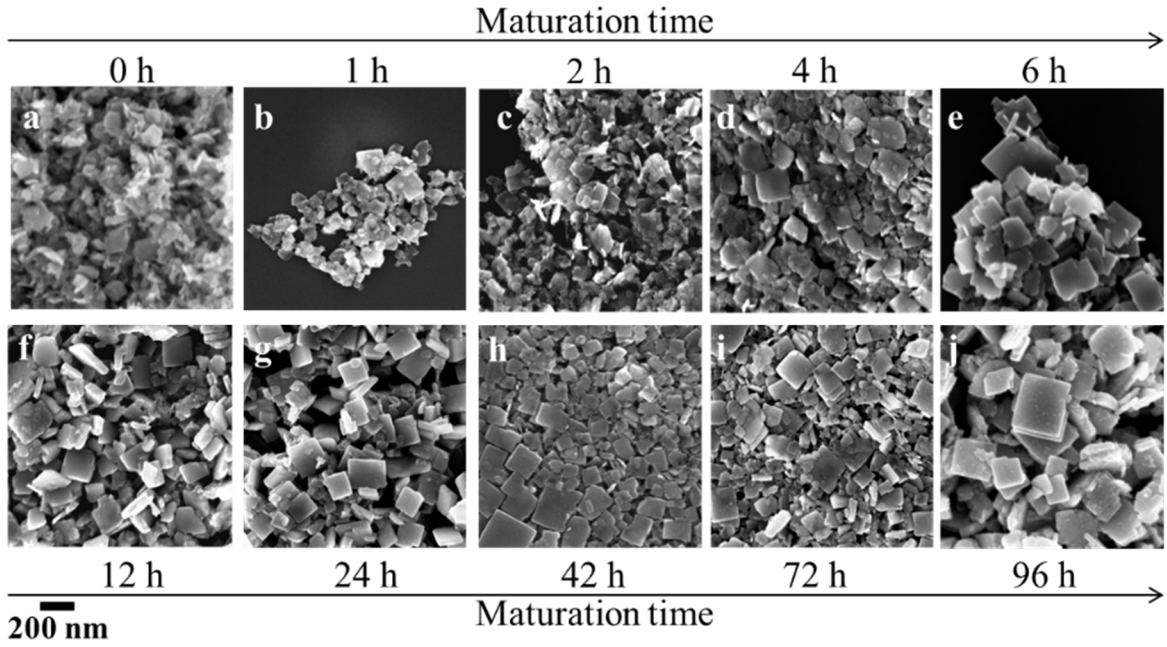

Fig. 4. SEM images of NP pristine material obtained after different maturation times (not calcined). The scale bare is the same for all images

Table. 3. Evolution of the NPs' lateral size during the aging step

Maturation Time (h)	**4**	**6**	**12**	**24**	**42**	**72**	**96**
Lateral size (nm)	190 ± 48	199 ± 51	170 ± 43	167 ± 26	168 ± 50	178 ± 93	166 ± 33

Such a 2D morphology of the tungstite powder obtained using an acid precipitation method was also reported by Ahmadi and co-workers [32], who prepared tungstite nanoribbons that retained their 2D morphology after dehydration. According to these authors, after the protonation of the tungstate ions, hydration of the $[WO_2(OH)_2]$ tetrahedral molecules occurs, followed by dimerization via O-bridging of the $[WO(OH)_3(H_2O)]$ molecules to form crystalline $[WO(OH)_3(H_2O)]_2(\mu\text{-}O)$. Whatever the calcination temperature until 800°C, they obtained γ-WO_3 while our NP sample undergoes a non-reversible γ- to β-phase transition for calcination at 500°C. Two major differences could be identified between their synthesis parameters and ours, which are the temperature and the pH of the ageing step and could explain the obtained morphological variation. Their precipitates were allowed to age at ambient temperature in pure water after washing, while ours were aged at 80°C in 2M hydrochloric acid. Although the growth habit of tungstite crystal is mainly determined by its intrinsic structure, it is also affected

by the external solution conditions such as concentration of reactants, temperature and pH, as shown by Huang and co-workers [41]. So pH and temperature may affect the dimerization or oxolation process during maturation, leading to different 2D morphologies (square nanoplates or nanoribbons).

For PS, the growth process occurs directly by crystallite formation in one step after obtaining the xerogel. Unlike NP, no maturation time is required. The growth mechanism occurred by the addition of nitric acid (HNO_3, 70%) to the ammonium paratungstate solution dissolved in ethanol which leads to the formation of the first hydrated tungsten oxide seeds. These germs surrounded by ethanol tend to reduce their surface by aggregating with other germs and give rise to larger particles in a pseudo-spherical shape. The growth mechanism is depicted in Fig. 5.

Finally, the thermal calcination of both morphologies allows both the removal of residual water and a crystallization.

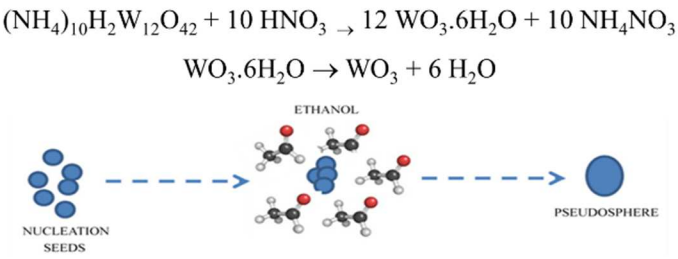

Fig. 5. Equation and schematic mechanism of PS formation

3.3. *Optical properties*

The optical characteristic of the produced materials was obtained by diffuse reflectance UV-Vis/near-IR spectroscopy at room temperature. The Fig. 6 shows the optical absorption spectra for NP and PS oxides calcined at different temperatures. The spectra indicate absorption onsets from 490-530 nm (equivalent to 2.53 – 2.34 eV) for NP and from 493-552 nm for PS (equivalent to 2.52 – 2.25 eV). According to these results, our samples are suitable for absorption in the visible light region of the spectra. For comparison, TiO_2 nanoparticles showed an absorption onset at 380 nm, which corresponds to the UV light region of the spectra.

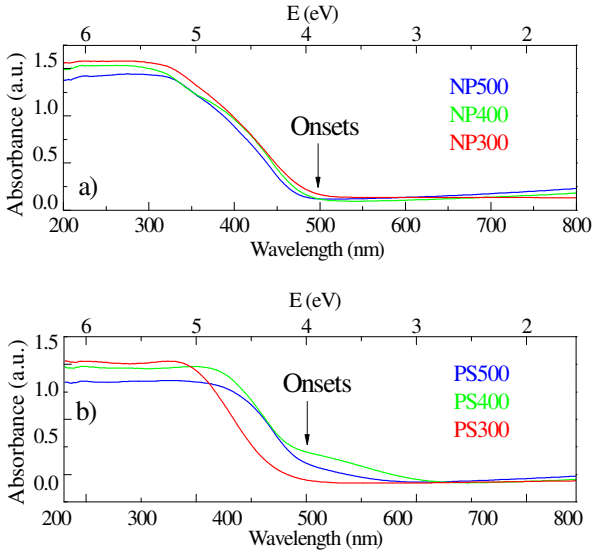

Fig. 6. Optical absorption spectra of the synthesized powders at room temperature, a) NP and b) PS

The absorption properties depend on the photon energy (hν) ranges compared to the band gap energy. For $h\nu > E_g$, absorption is mainly due to the charged transition linked to defects, like oxygen vacancies [42]. For $h\nu < E_g$, the absorption is due to the transition of electrons from the occupied states of the valence band to unoccupied states of the conduction band.

3.4. *Band gap energy*

Generally, the photosensitivity properties of materials depend on the absorption and band gap energies (Eg). Furthermore, several parameters such as the morphology and thermal treatment, also have an influence on optical properties. To calculate the band gap energy, we used a Kubelka-Munk method for an indirect semiconductor by plotting $[F(R_\infty)*E]^{1/2}$ versus photon energy. The band gap can be deduced from a linear part of the spectra using a linear fitting method. R_∞ indicates the absolute reflectance of the sample at infinite thickness and $F(R_\infty)$ is the conversion of the diffuse reflectance measurements R_∞ to $F(R_\infty)$ according to the $F(R_\infty) = (1-R_\infty)^2/2R_\infty$ equation. $[F(R_\infty)*E]^{1/2}$ of the samples at different calcining temperatures are plotted in Fig. 7.

The band gap energy for NP morphology is not drastically impacted with the different calcination temperatures. It was expected according to the thermal analysis which shows a well crystallization degree obtained from 300°C. By contrast, PS sample has a band gap energy which decreases when temperature increases with 2.43 eV at 500°C and 2.72 eV at 300°C. The low band gap can be attributed to the fact that the as-prepared samples possess defects, oxygen vacancies which can generate localized states in the band gap. The increase in band gap with

temperature can be attributed to the reduction of oxygen vacancies and the disappearance of the associated energy levels. In the case of semiconducting materials [43], the band gaps increase as crystallite sizes decrease (i.e. treatment temperature increases). The band gap values are consistent with reported ones for monoclinic and orthorhombic WO_3 [42,44–46]

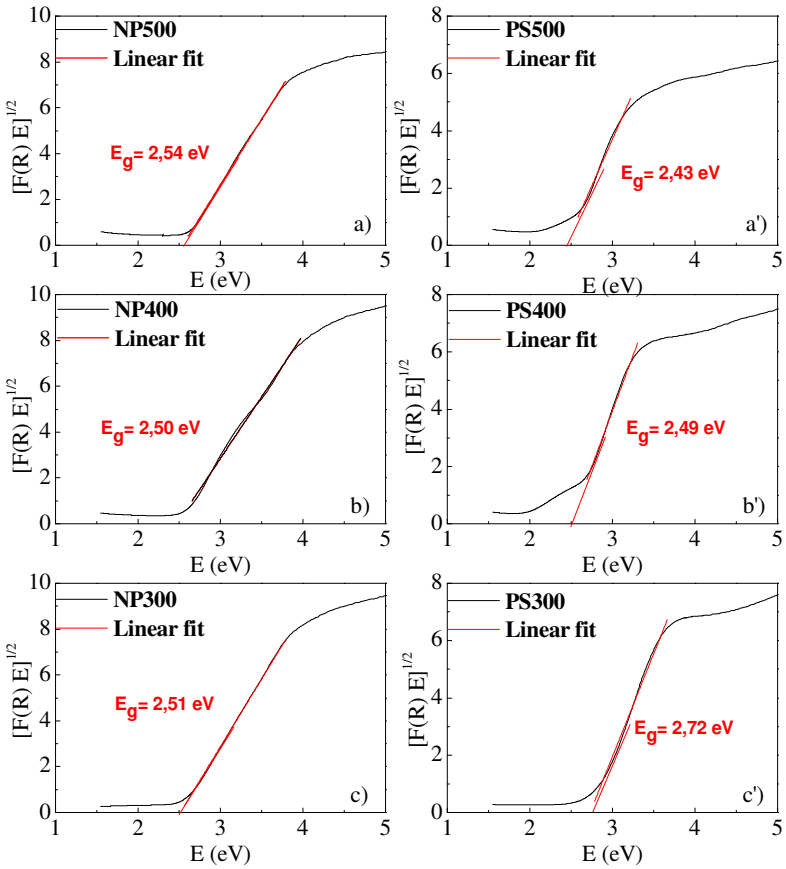

Fig. 7. Kubelka-Munk method to determinate bandgap energy of a) NP500, b) NP400, c) NP300 and a') PS500, b') PS400, c') PS300

The band gap is dependent on bonding-antibonding interactions, as a function of orbital overlap in each direction. The variations can be attributed to different factors, such as the degree of structural order-disorder induced by thermal treatments, lattice parameters, crystallite sizes, defects and shapes [47,48]. These factors depend on polyhedral distortion as reported in previous work (NP and PS at 500°C). The bond length and angles vary according to morphology and temperature treatment [32]. Furthermore, there are several distortions with phase ordering through the monoclinic to orthorhombic transition [38]. Chatten et al. reported a change in the band structure according to the phase present. The orthorhombic system shows successive long-short W-O bonds in the y and z directions. But the monoclinic phase exhibits W-O long-short splitting in all three directions. The splitting is stronger in the monoclinic system than the

orthorhombic. Consequently, the magnitude of the band gap is dominated by the splitting in each direction.

3.5. *Photocatalytic application*

The photocatalytic activities of the as-prepared powders were investigated by MB-dye photodegradation under solar light at room temperature and the natural pH of MB–WO_3 catalyst solution. Fig. 8 shows an example of UV-Vis spectra of the PS500 during the adsorption step in the darkness (Fig. 8a) and under solar light irradiation (Fig. 8b). For each analysis, we observed the decrease in intensities of all characteristic absorption bands, both during the adsorption and decomposition of MB.

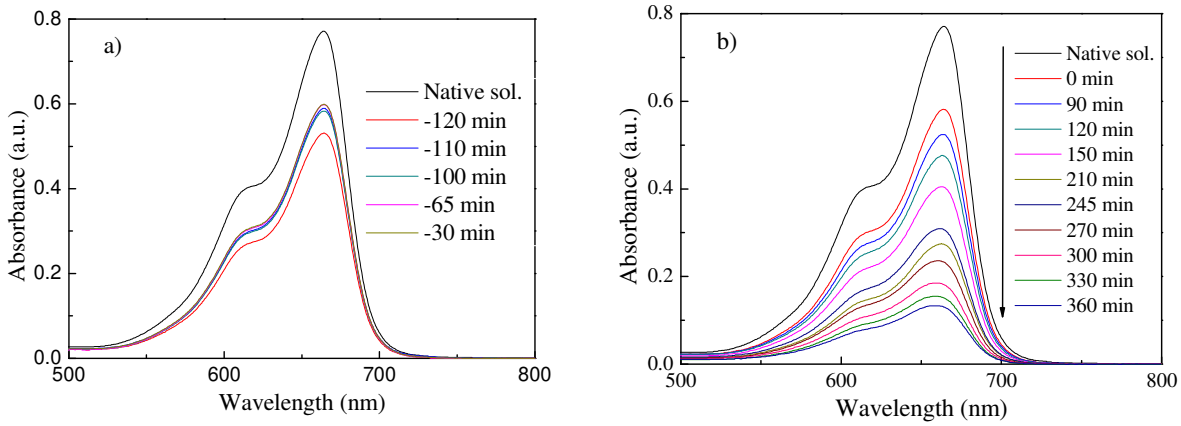

Fig. 8. An example of UV-Vis spectra during a) adsorption (darkness) and b) photocatalytic process (under solar light) of PS500

The temporal photocatalytic evaluation was obtained by plotting the evolution of the MB concentration (deduced from the absorbance at 664 nm, corresponding to the MB-dye's maximum wavelength), versus irradiation time. Fig. 9a,c) corresponds to the adsorption phenomenon which occurs in the darkness and Fig. 9b,d) corresponds to the photoinduction effect under solar light irradiation. The MB concentration at t_0 is the one which was obtained after adsorption-desorption equilibrium. In order to better understand the influence of two degradation's phenomena: photolysis in absence of photocatalyst, and photocatalysis in presence of different photocatalyst powders,a photolysis experiment was also performed (black plots in Fig. 9b and d) in the same conditions than the photocatalytic tests.

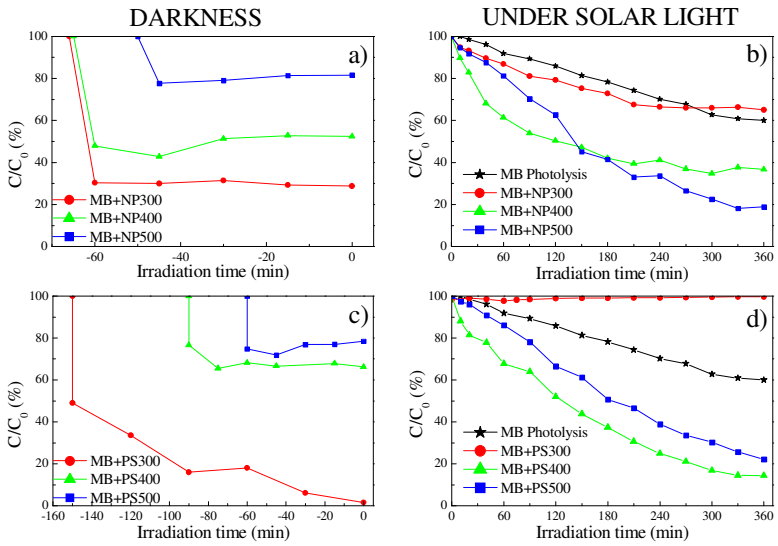

Fig. 9. Adsorption and photocatalysis rate of MB on WO_3 surfaces at different calcined temperatures: a, b) NP and c, d) PS

Photolysis leads to a degradation rate of roughly 40% over 360 min. Fig. 9a, c) show that the adsorption phenomenon occurs almost immediately in the first few minutes after mixing the solution with the catalyst and the adsorption-desorption equilibrium plateau is reached after 30 min of stirring (excepted for PS300). This corresponds to the saturation of the active sites which are available on the catalyst surface. The adsorption rate increases with decreasing sample calcination temperature of the sample. As expected, the thermal treatment induces an increase of the crystallite size, i.e. decrease of the surface area. This change results that the PS powder possesses a higher adsorption capacity than NP, particularly at lower temperatures. The strong adsorption of WO_3 can be due to the attractive interaction between the negative state charge (evidenced by zeta potential) and the cationic MB dye.

Overall, it appears in Fig. 9 that a calcination temperature of 300°C is not sufficient to limit adsorption phenomenon, thus resulting in high adsorption rates of 70% for NP and 100% for PS. With such high adsorption rates, it is obvious that the photoinduction process is not significant. About the two others calcination temperatures, it is apparent that the NP grains treated at 500°C are more efficient with a lower adsorption and a better photocatalytic activity with a degradation rate reaching 80% against only 60% for NP400. This could be explained by the particles size evolution which is triplet when calcination temperature is increased from 400°C (average of 188 nm) to 500°C (average of 612 nm). Increasing the NP size leads to a lower specific area which limits the number of available active sites at the surface of the

photocatalyst. For PS morphology, the adsorption rates are rather similar but PS400 is more catalytically efficient under solar light irradiation than PS500. According to the band gap energy, Eg(PS400) is higher than Eg(PS500) which leads to a longer charge carrier recombination time and an improvement of photoinduction activity. Therefore, the photocatalytic process is better for PS than NP grains, with a lower adsorption effect and a degradation after 360 min under irradiation reaching 88% for PS400 in comparison to 70% for NP500. This trend is confirmed by the high velocity constant of the degradation phenomenon (cf. Fig. S6; S7 ESI).

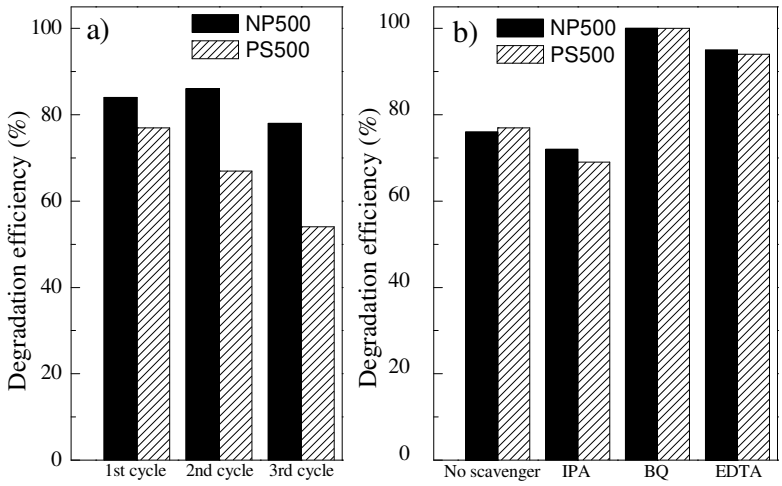

Fig. 10. a) Cycling curves of the photodegradation of MB-dye with PS- and NP500 for 3 cycles, b) The effect of different scavengers on the degradation of MB-dye

As reported in the literature [23,27], the photodecomposition reactions were based on three actives species such as superoxide radicals ($*O_2^-$), hydroxyl radicals (*OH) and holes (h^+). Fig. 10b) presents trapping results by IPA, BQ and EDTA-2Na for *OH, $*O_2^-$ and h^+, respectively. There is no significant difference between the two shapes (NP and PS) but it is possible to see that *OH are the major radicals responsible of the photodegradation. When we consumed h^+ and $*O_2^-$ by scavenger solutions, the degradation rate is notably improved which could be explained by *i)* a competition between two or three different degradation mechanisms depending on the implied active species and *ii)* a significantly more efficient mechanism resulting from the action of *OH than $*O_2^-$ and h^+. To verify this hypothesis, it is necessary to study in the future the degradation mechanism of the dye.

Apart from its photocatalytic activity, the stability of a photocatalyst is also prominent for its supportable recyclability. Fig. 10a) displays the recycling tests for the degradation of MB

dye over PS and NP treated at 500°C under solar light irradiation. While no noticeable loss in photocatalytic activity was perceived after three consecutive cycles for NP, the degradation efficiency is significantly decreased for PS. Thus, NP proved to be more stable than PS.

3.6. *Photosensitive properties*

The photocatalytic process is mainly based on the photon-catalyst interaction. The photocatalyst efficiency is not only due to the structural and morphological characteristics but also due to the rate of the photogenerated electron/hole pairs. Their population corresponds to the effectiveness of the catalyst in transferring charge carriers to O_2 and OH^- to form oxidizing radicals OH*. To highlight these aspects of charge transfer, photoluminescence (PL) and photoresistance (PR) properties were studied, using samples treated at 500°C, which showed the lowest adsorption rate and good photocatalytic yield.

3.6.1. *Photoluminescence*

To investigate the photogenerated electron-hole pair separation ability of NP and PS, we used PL approach. The PL spectra of both samples are shown in Fig. 11. Both WO_3 NP and PS are photoluminescent compounds, showing a large emission band centred at 605 and 643 nm, respectively. Fig. 11 presents the deconvolution of the PL spectra, with three curves at 500 (green), 560 (green) and 660 nm (red). The strong emission peaks are induced by the electron-hole radiative recombination, which is due to the de-excitation from W^{6+} (4f) to O^{2-} (2p). However, the shoulders were caused by the localized state in the band gap due to the impurities. Those identified near 500 nm, represent the emission of the excited electron in the W^{5+} to O^{2-} in the octahedral cluster [WO_6] [42,49,50]. The NP powders present an intensity three times more significant than PS particles and the shift of the main emission band is identical to the green emission band at 540 nm. This trend indicates the lower recombination rate of the photoinduced electron-hole pairs due to the formation of a Schottky barrier. The functions of the Schottky junction accelerate the separation and the transfer of the photogenerated charge, which could lead to high photocatalytic activities [25,51,52].

Generally, the difference in emission spectra can be due to the combination of several parameters, like phase purity (defects like oxygen vacancies), polyhedral distortion, crystallite size and morphology, which depend on the experimental conditions.

The PL properties are an interesting way to study photocatalysis, which demonstrates the capability to modify the quenching recombination of exciting conditions. The low PL intensity

for PS nanoparticles can induce a low recombination rate of photogenerated charges carriers under light irradiation [53]. Then, the charges carriers can react on the catalyst surface, such that not only are the hydroxyl radicals formed from the holes but also from the electrons. In fact, the power for e– to generate OH* is much weaker than that of h^+, then the photogenerated holes form highly reactive hydroxyl radicals give rise to a strong photocatalytic activity. The reactions that occur during the photocatalytic process result in an efficient separation of the photogenerated electron/hole pairs, which play a central role in the photodegradation of MB.

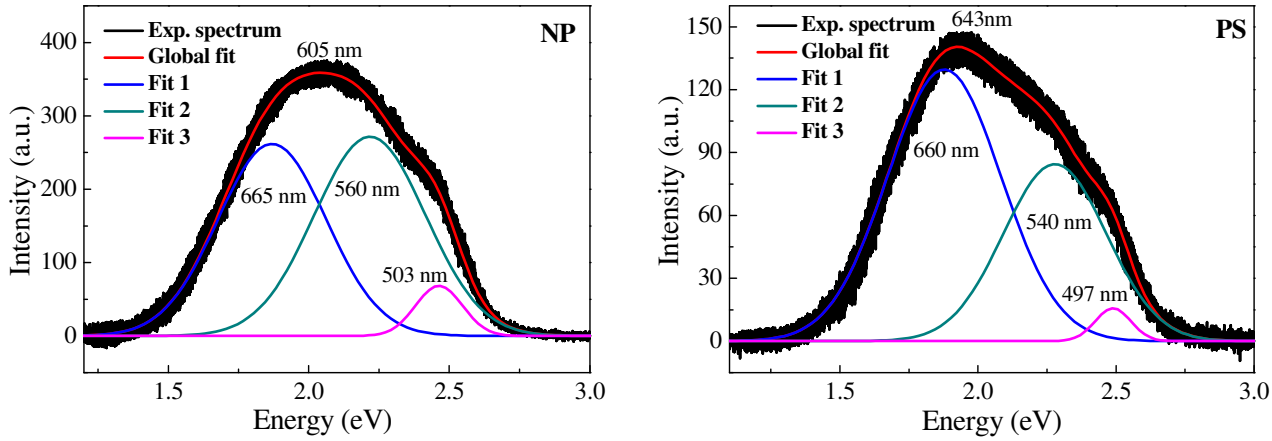

Fig. 11. Photoluminescence spectra with deconvolution peaks of NP and PS

3.6.2. Photoresistance

The effects of the grain size and morphology on the photocatalytic activity process can be revealed by the electronic properties of the photocatalyst. In addition to the PL investigations, we used the PR to probe the charge carriers transfers under solar light irradiation. The corresponding PR responses to light on-off cycling are shown in Fig. 12. Under light exposure, the resistance of both samples decreased rapidly to a plateau in only 90 sec and remained constant under continuous irradiation. As expected, there is a high number of photogenerated electron-hole pairs for both samples, if we maintain the irradiation. However, in the darkness, the NP and PS samples photoresistance behave differently. Just after switching off the light, the PS resistance starts to increase up to its baseline, over 150 min. Regarding the NP photoresponse, the resistance remains almost flat for 60 minutes with a slight increase, giving rise to a deaccumulation of excess electrons. After that, we observe a sharp increase in resistance, corresponding to the two-third of the signal intensity, then we reach the starting resistance after 20 minutes. This difference in PR trend can be due to several parameters such as the degree of crystallization, grain sizes, shapes and defects.

As reported in the literature, the increase of the band gap favors the photoactivity process, because the photogenerated electrons are maintained in the conduction band and recombination with holes is delayed. As shown in the PR profiles, the electrons lifetime is rather more prolonged in the NP than PS particles for the first 60 minutes. However, over 75 minutes, the starting NP resistance is reached while electrons are still confined in the PS conduction band. Regarding the photocatalytic activity, the photoinduced decomposition process occurs over 360 min and PS has better activity than NP, especially those treated at 500°C. This agrees with the lifetime of the charge carriers, observed after 75 minutes of light exposure. In this case, the non-recombined electron-hole pairs can be transferred respectively to O_2 and to OH thus producing O_2^- superoxide anion and HO* hydroxylic radicals. The active species produced in the previous process will degrade the pollutant as discussed with PL properties. [28].

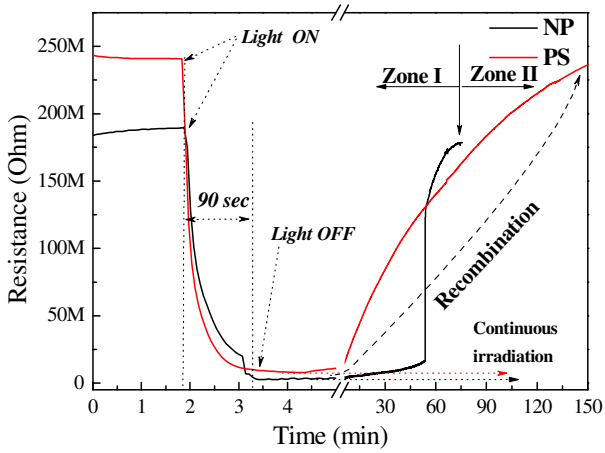

Fig. 12. Comparison of photoresistance responses to light On-Off of NP (a, b and c) and PS (d, e and f)

4. Conclusion

The dependencies of the photosensitive properties of WO_3 were investigated using two morphologies, nanoplatelets and pseudospheres. Thermal treatment revealed two crystallization phases, a monoclinic phase at 400°C and an orthorhombic phase at 500°C. The photocatalytic activity showed different efficiencies for both morphologies. It depends on the calcination temperatures, as the degradation process is composed of a strong adsorption at low temperature followed by a photoinduced decomposition. Good crystallization at 400°C and 500°C displayed higher photocatalytic activity, reaching 70% and 88% for NP and PS, respectively. The scavengers study indicated that the OH* is the dominating active species in the photodegradation process for both samples, but recycling experiments of NP showed higher photocatalytic stability than PS. The optical properties showed a band gap varying from 2.49 – 2.72 eV, allowing an absorption in the visible light region of the spectra. The role of the particle

morphology and size is evidenced by PL and PR investigation. The PS500 showed a lower PL intensity and a long-time recombination from PR analysis compared to NP500, demonstrating electron-hole separation and interface charge transfers on WO_3.

Acknowledgments

We gratefully acknowledge the Regional Council of Provence-Alpes-Côte d'Azur, General Council of Var, and the urban community of Toulon Provence Mediterranean for their financial support in the framework of the "NPPSE" project.

References

[1 D. Robert, N. Keller, et E. Selli, « Environmental photocatalysis and photochemistry for a sustainable world: a big challenge », 2017.
[2] Y. Sang, H. Liu, A. Umar, Photocatalysis from UV/Vis to Near-Infrared Light: Towards Full Solar-Light Spectrum Activity, ChemCatChem. 7 (2015) 559–573.
[3] Z.W. Pan, Z.R. Dai, Z.L. Wang, Nanobelts of Semiconducting Oxides, Science. 291 (2001) 1947–1949. doi:10.1126/science.1058120.
[4] U. Chalapathi, B. Poornaprakash, S.-H. Park, Growth and properties of cubic SnS films prepared by chemical bath deposition using EDTA as the complexing agent, Journal of Alloys and Compounds. 689 (2016) 938–944. doi:10.1016/j.jallcom.2016.08.066.
[5] D. Pourjafari, D. Reyes-Coronado, A. Vega-Poot, R. Escalante, D. Kirkconnell-Reyes, R. García-Rodríguez, J.A. Anta, G. Oskam, Brookite-Based Dye-Sensitized Solar Cells: Influence of Morphology and Surface Chemistry on Cell Performance, J. Phys. Chem. C. 122 (2018) 14277–14288. doi:10.1021/acs.jpcc.8b02384.
[6] X. Yuan, J. Yang, J. He, H.H. Tan, C. Jagadish, Role of surface energy in nanowire growth, J. Phys. D: Appl. Phys. 51 (2018) 283002. doi:10.1088/1361-6463/aac9f4.
[7] C.-Y. Nam, D. Su, C.T. Black, High-Performance Air-Processed Polymer–Fullerene Bulk Heterojunction Solar Cells, Advanced Functional Materials. 19 (2009) 3552–3559. doi:10.1002/adfm.200900311.
[8] Y. Zheng, Z. Wang, Y. Tian, Y. Qu, S. Li, D. An, X. Chen, S. Guan, Synthesis and performance of 1D and 2D copper borate nano/microstructures with different morphologies, Colloids and Surfaces A: Physicochemical and Engineering Aspects. 349 (2009) 156–161. doi:10.1016/j.colsurfa.2009.08.012.
[9] X.-L. Li, T.-J. Lou, X.-M. Sun, Y.-D. Li, Highly Sensitive WO3 Hollow-Sphere Gas Sensors, Inorg. Chem. 43 (2004) 5442–5449. doi:10.1021/ic049522w.
[10] S. Wang, W. Fan, Z. Liu, A. Yu, X. Jiang, Advances on Tungsten Oxide Based Photochromic Materials: Strategies to Improve Photochromic Properties, Journal of Materials Chemistry C. (2017).
[11] S.V. Mohite, V.V. Ganbavle, K.Y. Rajpure, Solar photoelectrocatalytic activities of rhodamine-B using sprayed WO3 photoelectrode, Journal of Alloys and Compounds. 655 (2016) 106–113. doi:10.1016/j.jallcom.2015.09.154.
[12] F. Chen, H. Huang, L. Ye, T. Zhang, Y. Zhang, X. Han, T. Ma, Thickness-Dependent Facet Junction Control of Layered BiOIO3 Single Crystals for Highly Efficient CO2 Photoreduction, Advanced Functional Materials. 28 (2018) 1804284. doi:10.1002/adfm.201804284.
[13] F. Liu, L. Li, F. Mo, J. Chen, S. Deng, N. Xu, A Catalyzed-Growth Route to Directly Form Micropatterned WO2 and WO3 Nanowire Arrays with Excellent Field Emission

Behaviors at Low Temperature, Crystal Growth & Design. 10 (2010) 5193–5199. doi:10.1021/cg100995f.
[14] S. Nishimoto, T. Mano, Y. Kameshima, M. Miyake, Photocatalytic water treatment over WO3 under visible light irradiation combined with ozonation, Chemical Physics Letters. 500 (2010) 86–89. doi:10.1016/j.cplett.2010.09.086.
[15] H. Yu, J. Li, Y. Zhang, S. Yang, K. Han, F. Dong, T. Ma, H. Huang, Three-in-one oxygen vacancy: whole visible-spectrum absorption, efficient charge separation and surface site activation for robust CO2 photoreduction, Angewandte Chemie International Edition. (2019).
[16] X. Wu, S. Yao, Flexible electrode materials based on WO3 nanotube bundles for high performance energy storage devices, Nano Energy. 42 (2017) 143–150.
[17] H. Zheng, J.Z. Ou, M.S. Strano, R.B. Kaner, A. Mitchell, K. Kalantar-zadeh, Nanostructured tungsten oxide–properties, synthesis, and applications, Advanced Functional Materials. 21 (2011) 2175–2196.
[18] A. Alinsafi, F. Evenou, E.M. Abdulkarim, M.N. Pons, O. Zahraa, A. Benhammou, A. Yaacoubi, A. Nejmeddine, Treatment of textile industry wastewater by supported photocatalysis, Dyes and Pigments. 74 (2007) 439–445. doi:10.1016/j.dyepig.2006.02.024.
[19] C. Hachem, F. Bocquillon, O. Zahraa, M. Bouchy, Decolourization of textile industry wastewater by the photocatalytic degradation process, Dyes and Pigments. 49 (2001) 117–125. doi:10.1016/S0143-7208(01)00014-6.
[20] M. Alaei, A.R. Mahjoub, A. Rashidi, Effect of WO3 Nanoparticles on Congo Red and Rhodamine B Photo Degradation, Iranian Journal of Chemistry and Chemical Engineering (IJCCE). 31 (2012) 23–29.
[21] Q. Sun, F. Xiao, S. Ren, Z. Dong, J. Wang, X. Su, Hydrothermal synthesis of WO3 nanorods and their performance in the adsorption of Rhodamine B and the synthesis of adipic acid, Ceramics International. 40 (2014) 11447–11451. doi:10.1016/j.ceramint.2014.03.151.
[22] Y. Lu, G. Liu, J. Zhang, Z. Feng, C. Li, Z. Li, Fabrication of a monoclinic/hexagonal junction in WO3 and its enhanced photocatalytic degradation of rhodamine B, Chinese Journal of Catalysis. 37 (2016) 349–358. doi:10.1016/S1872-2067(15)61023-3.
[23] H. Huang, X. Han, X. Li, S. Wang, P.K. Chu, Y. Zhang, Fabrication of Multiple Heterojunctions with Tunable Visible-Light-Active Photocatalytic Reactivity in BiOBr–BiOI Full-Range Composites Based on Microstructure Modulation and Band Structures, ACS Appl. Mater. Interfaces. 7 (2015) 482–492. doi:10.1021/am5065409.
[24] X. Wang, L. Pang, X. Hu, N. Han, Fabrication of ion doped WO3 photocatalysts through bulk and surface doping, Journal of Environmental Sciences. 35 (2015) 76–82. doi:10.1016/j.jes.2015.04.007.
[25] J. Zhang, X. Fu, H. Hao, W. Gan, Facile synthesis 3D flower-like Ag@WO3 nanostructures and applications in solar-light photocatalysis, Journal of Alloys and Compounds. 757 (2018) 134–141. doi:10.1016/j.jallcom.2018.05.068.
[26] I. Aslam, C. Cao, W.S. Khan, M. Tanveer, M. Abid, F. Idrees, R. Riasat, M. Tahir, F.K. Butt, Z. Ali, Synthesis of three-dimensional WO3 octahedra: characterization, optical and efficient photocatalytic properties, RSC Adv. 4 (2014) 37914–37920. doi:10.1039/C4RA05724D.
[27] M. Elnouby, A.A. El-Hamid, H.M. Soliman, Adsorption of methylene blue dye on tungsten oxide nanoplates, (n.d.).
[28] I. Vamvasakis, I. Georgaki, D. Vernardou, G. Kenanakis, N. Katsarakis, Synthesis of WO3 catalytic powders: evaluation of photocatalytic activity under NUV/visible light

irradiation and alkaline reaction pH, J Sol-Gel Sci Technol. 76 (2015) 120–128. doi:10.1007/s10971-015-3758-5.
[29] S. Adhikari, S. Mandal, D. Sarkar, D.-H. Kim, G. Madras, Kinetics and mechanism of dye adsorption on WO3 nanoparticles, Applied Surface Science. 420 (2017) 472–482. doi:10.1016/j.apsusc.2017.05.191.
[30] G. Guan, J. Xia, S. Liu, Y. Cheng, S. Bai, S.Y. Tee, Y.-W. Zhang, M.-Y. Han, Electrostatic-Driven Exfoliation and Hybridization of 2D Nanomaterials, Advanced Materials. 29 (2017) 1700326. doi:10.1002/adma.201700326.
[31] N. Dirany, M. Arab, C. Leroux, S. Villain, V. Madigou, J. Gavarri, Effect of WO3 nanoparticles morphology on the catalytic properties, Materials Today: Proceedings. 3 (2016) 230–234.
[32] N. Dirany, M. Arab, V. Madigou, C. Leroux, J.R. Gavarri, A facile one step route to synthesize WO3 nanoplatelets for CO oxidation and photodegradation of RhB: microstructural, optical and electrical studies, RSC Adv. 6 (2016) 69615–69626. doi:10.1039/C6RA13500E.
[33] M. Ahmadi, S. Sahoo, R. Younesi, A.P.S. Gaur, R.S. Katiyar, M.J.-F. Guinel, WO3 nanoribbons: their phase transformation from tungstite (WO3·H2O) to tungsten oxide (WO3), J Mater Sci. 49 (2014) 5899–5909. doi:10.1007/s10853-014-8304-2.
[34] T. Vogt, P.M. Woodward, B.A. Hunter, The High-Temperature Phases of WO3, Journal of Solid State Chemistry. 144 (1999) 209–215. doi:10.1006/jssc.1999.8173.
[35] P. Roussel, P. Labbé, D. Groult, Symmetry and twins in the monophosphate tungsten bronze series (PO2)4(WO3)2m ($2 \leq m \leq 14$), Acta Cryst B, Acta Cryst Sect B, Acta Crystallogr B, Acta Crystallogr Sect B, Acta Crystallogr Struct Sci, Acta Crystallogr Sect B Struct Sci, Acta Crystallogr B Struct Sci Cryst Eng Mater. 56 (2000) 377–391. doi:10.1107/S0108768199016195.
[36] E. Salje, The orthorhombic phase of WO3, Acta Crystallographica Section B. 33 (1977) 574–577. doi:10.1107/S0567740877004130.
[37] M. Boulova, N. Rosman, P. Bouvier, G. Lucazeau, High-pressure Raman study of microcrystalline WO 3 tungsten oxide, J. Phys.: Condens. Matter. 14 (2002) 5849. doi:10.1088/0953-8984/14/23/314.
[38] A.Z. Sadek, H. Zheng, M. Breedon, V. Bansal, S.K. Bhargava, K. Latham, J. Zhu, L. Yu, Z. Hu, P.G. Spizzirri, W. Wlodarski, K. Kalantar-zadeh, High-Temperature Anodized WO3 Nanoplatelet Films for Photosensitive Devices, Langmuir. 25 (2009) 9545–9551. doi:10.1021/la901944x.
[39] M. Yang, N.K. Shrestha, P. Schmuki, Thick porous tungsten trioxide films by anodization of tungsten in fluoride containing phosphoric acid electrolyte, Electrochemistry Communications. 11 (2009) 1908–1911. doi:10.1016/j.elecom.2009.08.014.
[40] C. Ng, C. Ye, Y.H. Ng, R. Amal, Flower-Shaped Tungsten Oxide with Inorganic Fullerene-like Structure: Synthesis and Characterization, Crystal Growth & Design. 10 (2010) 3794–3801. doi:10.1021/cg100625m.
[41] J. Huang, X. Xu, C. Gu, M. Yang, M. Yang, J. Liu, Large-scale synthesis of hydrated tungsten oxide 3D architectures by a simple chemical solution route and their gas-sensing properties, J. Mater. Chem. 21 (2011) 13283–13289. doi:10.1039/C1JM11292A.
[42] R. Chatten, A.V. Chadwick, A. Rougier, P.J.D. Lindan, The Oxygen Vacancy in Crystal Phases of WO3, J. Phys. Chem. B. 109 (2005) 3146–3156. doi:10.1021/jp045655r.
[43] A.P. Alivisatos, Semiconductor Clusters, Nanocrystals, and Quantum Dots, Science. 271 (1996) 933–937. doi:10.1126/science.271.5251.933.
[44] S. Vidya, S. Solomon, J.K. Thomas, Synthesis and characterisation of MoO3 and WO3 nanorods for low temperature co-fired ceramic and optical applications, J Mater Sci: Mater Electron. 26 (2015) 3243–3255. doi:10.1007/s10854-015-2823-8.

[45] S.B. Patil, S.R. Mane, V.R. Patil, R.R. Kharade, P.N. Bhosale, Chemosynthesis and characterization of electrochromic vanadium doped molybdenum oxide thin films, Applied Science Research 3. 3 (2011) 481–491.
[46] Y. Zhao, J. Liu, Y. Zhou, Z. Zhang, Y. Xu, H. Naramoto, S. Yamamoto, Preparation of MoO 3 nanostructures and their optical properties, J. Phys.: Condens. Matter. 15 (2003) L547. doi:10.1088/0953-8984/15/35/101.
[47] I.L.V. Rosa, A.P.A. Marques, M.T.S. Tanaka, D.M.A. Melo, E.R. Leite, E. Longo, J.A. Varela, Synthesis, Characterization and Photophysical Properties of Eu3+ Doped in BaMoO4, J Fluoresc. 18 (2008) 239–245. doi:10.1007/s10895-007-0195-z.
[48] R. Lacomba-Perales, J. Ruiz-Fuertes, D. Errandonea, D. Martínez-García, A. Segura, Optical absorption of divalent metal tungstates: Correlation between the band-gap energy and the cation ionic radius, EPL. 83 (2008) 37002. doi:10.1209/0295-5075/83/37002.
[49] S.-H. Lee, H.M. Cheong, J.-G. Zhang, A. Mascarenhas, D.K. Benson, S.K. Deb, Electrochromic mechanism in a-WO3−y thin films, Appl. Phys. Lett. 74 (1999) 242–244. doi:10.1063/1.123268.
[50] S.-H. Lee, H.M. Cheong, C.E. Tracy, A. Mascarenhas, A.W. Czanderna, S.K. Deb, Electrochromic coloration efficiency of a-WO 3− y thin films as a function of oxygen deficiency, Applied Physics Letters. 75 (1999) 1541–1543.
[51] S.-F. Yang, C.-G. Niu, D.-W. Huang, H. Zhang, C. Liang, G.-M. Zeng, SrTiO3 nanocubes decorated with Ag/AgCl nanoparticles as photocatalysts with enhanced visible-light photocatalytic activity towards the degradation of dyes, phenol and bisphenol A, Environ. Sci.: Nano. 4 (2017) 585–595. doi:10.1039/C6EN00597G.
[52] M.A. Gondal, M.A. Suliman, M.A. Dastageer, G.-K. Chuah, C. Basheer, D. Yang, A. Suwaiyan, Visible light photocatalytic degradation of herbicide (Atrazine) using surface plasmon resonance induced in mesoporous Ag-WO3/SBA-15 composite, Journal of Molecular Catalysis A: Chemical. C (2016) 208–216. doi:10.1016/j.molcata.2016.10.015.
[53] L. Zhu, K. Liu, H. Li, Y. Sun, M. Qiu, Solvothermal synthesis of mesoporous TiO2 microspheres and their excellent photocatalytic performance under simulated sunlight irradiation, Solid State Sciences. 20 (2013) 8–14. doi:10.1016/j.solidstatesciences.2013.02.026.